Journal of Colloid and Interface Science 703 (2026) 139286

Contents lists available at ScienceDirect

Journal of Colloid And Interface Science

journal homepage: www.elsevier.com/locate/jcis

Regular Article

How lipids suppress cavitation in biological fluids

Marin Šako [a,b], Steven Jansen [c], H. Jochen Schenk [d], Roland R. Netz [e], Emanuel Schneck [f], Matej Kanduč [a,*]

[a] Jožef Stefan Institute, 1000 Ljubljana, Slovenia
[b] University of Ljubljana, Faculty of Mathematics and Physics, 1000 Ljubljana, Slovenia
[c] Institute of Botany, Ulm University, 89081 Ulm, Germany
[d] Department of Biological Science, California State University, Fullerton, CA 92831, USA
[e] Fachbereich Physik, Freie Universität Berlin, Berlin 14195, Germany
[f] Physics Department, Technische Universität Darmstadt, 64289 Darmstadt, Germany

GRAPHICAL ABSTRACT

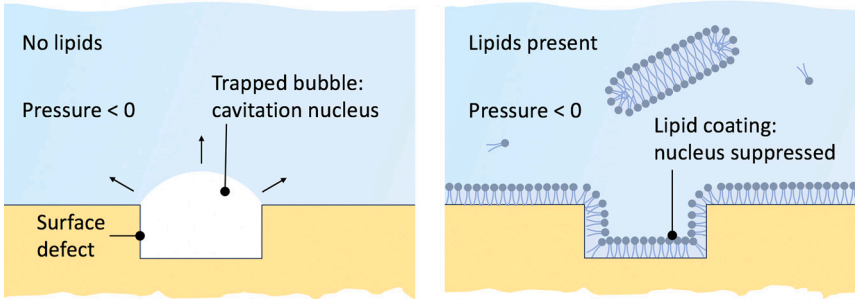

ARTICLE INFO

Dataset link: https://doi.org/10.5281/zenodo.15529899, https://doi.org/10.5281/zenodo.14678800

Keywords:
Cavitation
Lipid monolayer
Lipid bilayer
Bubble
Molecular dynamics simulation

ABSTRACT

Hypothesis: Cavitation in water under tension is often initiated at nanoscale hydrophobic surface defects that stabilize preexisting nanobubbles. We hypothesize that amphiphilic molecules, such as polar lipids, can adsorb onto these defects and suppress cavitation by removing nanobubble nucleation sites.
Simulations: To test this mechanism, we performed atomistic molecular dynamics simulations in combination with classical nucleation theory to model lipid bilayers and monolayer coatings at hydrophobic surfaces containing nanoscale pits and to investigate their response to applied negative pressures.
Findings: We find that lipids readily adsorb onto hydrophobic surfaces, conform to nanoscale features, and eliminate bubble-hosting cavities. This passivation shifts the cavitation-limiting step from nanobubble expansion at defects to rupture of lipid bilayers, which exhibit much higher cavitation resistance. These results provide a molecular basis for how amphiphilic additives enhance the stability of aqueous liquids against cavitation, even in the presence of unavoidable surface imperfections. This mechanism also offers a physically grounded explanation for how vascular plants sustain sap transport under substantial negative pressures despite structural heterogeneities in their water-conducting vessels.

* Corresponding author.
E-mail address: matej.kanduc@ijs.si (M. Kanduč).

https://doi.org/10.1016/j.jcis.2025.139286
Received 19 August 2025; Received in revised form 15 October 2025; Accepted 15 October 2025

Available online 16 October 2025

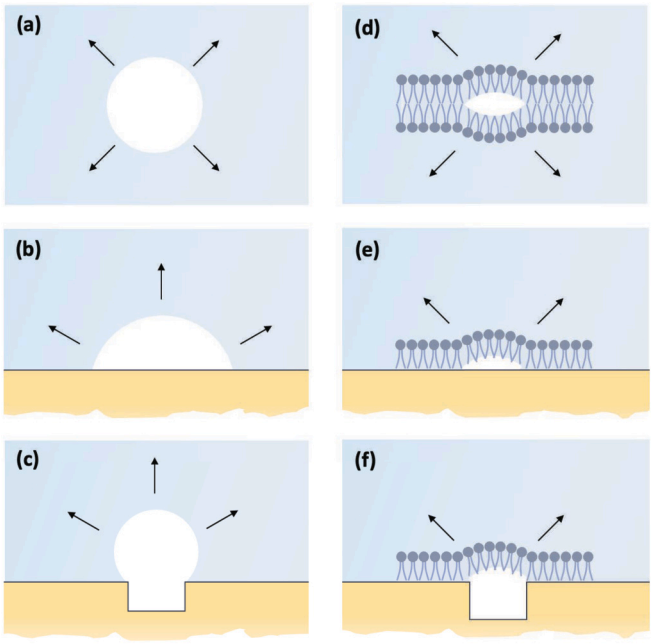

Fig. 1. Schematic overview of cavitation pathways considered in this work, combining existing literature and our new simulation results: (a) homogeneous cavitation in pure bulk water ($p_{cav} \sim -160$ to -110 MPa [18,19]); (b) heterogeneous cavitation at a smooth hydrophobic surface ($p_{cav} \sim -70$ to -60 MPa [16,17]); (c) expansion of a preexisting vapor bubble within a surface pit (p_{cav} scales inversely with the pit radius; see Eqs. (14) and (15) for details [20,21]); (d) cavitation via separation of lipid bilayer leaflets (concept introduced in Ref. [22], p_{cav} refined in this study); (e) cavitation in a lipid monolayer film adsorbed on a smooth surface (p_{cav} determined in this study); (f) cavitation of a lipid monolayer film at a surface pit, where lipids suppress pit-hosted nanobubbles (p_{cav} determined in this study).

1. Introduction

Water can sustain substantial negative pressure—also referred to as tension—for remarkably long times. Such metastable states are realized in a variety of systems: in plant xylem during transpiration-driven flow [1], in drying plant cells [2], in synthetic microfluidic devices [3,4], during nanopore wetting [5,6], or in acoustic cavitation experiments [7]. In vascular plants, sap is routinely transported under negative pressures, reaching down to −10 MPa in some species [1,8], generated by water evaporation from leaves. This remarkable feat enables trees to move the sap from the roots to the treetops without mechanical pumping.

At the same time, water under tension is in a thermodynamically metastable state and thus prone to cavitation—the sudden formation of vapor bubbles that rapidly expand. Cavitation is often undesirable: it can disrupt flow, damage materials, and lead to embolism and loss of hydraulic function in biological systems such as plants. The threshold for cavitation depends strongly on the nucleation pathway. Homogeneous cavitation in pure bulk water (as sketched in Fig. 1a) requires extreme negative pressures, generally between −160 to −110 MPa [9–14]. However, this nucleation pathway can only be reached under carefully controlled laboratory conditions, for example, in micron-sized hydrophilic containers [12,15]. Instead, cavitation typically proceeds via heterogeneous nucleation at surfaces or impurities (as shown in Fig. 1b). For instance, atomically smooth hydrophobic surfaces bring the cavitation threshold up to −70 to −60 MPa [16,17], while insoluble nonpolar aggregates increase it further to −30 MPa [14].

Geometrical irregularities on the surface, such as crevices, pits, and other concavities, can lead to even lower energy barriers for the formation of critical cavitation nuclei, especially when they host preexisting gas or vapor bubbles [20,21]. Whereas free gas bubbles suspended in bulk typically dissolve quickly, concave hydrophobic features can stabilize them—either as spontaneously dewetted vapor pockets or as trapped gas inclusions, commonly referred to as *Harvey nuclei* (Fig. 1c), a concept first proposed by Harvey et al. in 1944 [20]. Because of this Harvey-type nucleation pathway, water typically cavitates at pressures near the saturated vapor pressure—set by the size of the largest trapped bubble—despite its high theoretical bulk tensile strength in the absence of impurities [17,21,23–25].

While the expansion of such preexisting nanobubbles does not represent nucleation in the strict thermodynamic sense, as it does not involve the formation of a new phase, it still requires overcoming a free energy barrier and thus shares key features with classical nucleation, sometimes referred to as pseudo-classical nucleation [26]. For consistency with prior literature, we use the terms nucleation and cavitation to also include such bubble expansion mechanisms.

Achieving high tensile strengths in water, therefore, seems to require extreme purity: degassing, contaminant removal, and defect-free hydrophilic surfaces [9,11,27,28]. In practice, however, reaching defect-free conditions in large volumes is nearly impossible. Even a single hydrophobic defect that hosts a stable nanobubble can trigger cavitation at relatively modest negative pressures [17].

It is therefore remarkable that plant xylem conduits—macroscopic channels responsible for water transport—can sustain substantial negative pressures without immediate failure. After all, the sap they carry is far from pure water: it contains dissolved gases, organic molecules such as proteins, sugars, and lipids [29,30], and the xylem walls are not uniformly hydrophilic but contain hydrophobic heterogeneities [30–32]—factors that are expected to promote cavitation in physical systems.

Yet, despite these apparent vulnerabilities, plants maintain embolism-free sap transport over long distances and extended periods. Several studies suggest that naturally occurring amphiphiles may play a stabilizing role. Experiments have shown that adding alcohols [33], or even trace amounts of surfactants [34,35] or polymer additives [36], can suppress cavitation, remove bubbles from surfaces [37], and reduce damage caused by cavitation erosion [38]. Notably, siphon hoses treated with surfactants have been demonstrated to support water columns beyond the Torricellian limit (i.e., the maximum height achievable under atmospheric pressure *in equilibrium*, approximately 10 m), suggesting that negative pressures can be maintained without cavitation [39].

Direct experimental evidence for the surfactant-mediated suppression of cavitation remains limited, which is unsurprising given the challenges of controlling and characterizing nanoscopic cavitation nuclei. These nuclei are highly sensitive to surface topography, chemistry, and contamination, making reproducible experiments exceedingly difficult. Nevertheless, existing observations point toward a plausible mechanism: surfactants may inhibit cavitation by coating hydrophobic surfaces, passivating nucleation sites, and eliminating nanobubbles [30,32], although the precise mechanisms remain unclear. In the same vein, naturally occurring polar lipids in plant xylem may play a similar protective role. The primary lipids identified in the xylem sap are phospholipids and galactolipids, which coat lumen-facing vessel walls and pit membranes (mesoporous layers between xylem conduits) [30,32,40,41].

Above the critical vesiculation concentration (CVC), lipids self-assemble into bilayers in the bulk and adsorb as monolayers onto hydrophobic surfaces [42–46]. It is therefore plausible that lipids can passivate hydrophobic nucleation sites, but they may also introduce new cavitation-prone structures. For example, the two leaflets in a bilayer are held together by relatively weak adhesion interactions, and can separate under sufficient tension, giving rise to cavitation (Fig. 1d). Nonetheless, simulations suggest that bilayers can withstand the negative pressures typical of plant xylem [22]. The cavitation resistance of monolayer films on solid surfaces is even less well understood—particularly their ability to remain attached under tension, whether on generally smooth surfaces or at nanoscale defects, as illustrated in Figs. 1e and f.

The present study is motivated by these open questions and focuses on the role of lipid assemblies in modulating cavitation thresholds. We adopt a multi-scale approach, using molecular dynamics (MD) simulations to inform a framework based on classical nucleation theory (CNT) to systematically examine cavitation in lipid bilayers (Fig. 1d) and in lipid-coated hydrophobic surfaces (Fig. 1e), including those containing nanoscale defects (Fig. 1f). Our goal is to identify the weakest among these structures, which ultimately sets the cavitation threshold. Although inspired by plant xylem transport, our findings have broader implications for soft matter research, interfacial physics, and the design of long-lived metastable liquid systems under negative pressures.

2. Methods

2.1. Simulation model

Our approach consists of molecular-level modeling of water, dilauroylphosphatidylcholine (DLPC) lipids, and a smooth hydrophobic surface. For water, we used the TIP4P/2005 model [47], a four-site model known for accurately reproducing experimental interfacial tension (68 vs. 72 mN/m) and density (0.998 vs. 0.996 g/cm^3) at 300 K [45,48]. To simulate DLPC lipids, we chose the all-atom CHARMM36/LJ-PME force field [49], which was specifically optimized for Lennard-Jones (LJ) interactions treated via Particle–Mesh Ewald (PME) summation. This choice was motivated both by its demonstrated accuracy in modeling lipid bilayers [50] and by our own benchmarking with liquid decane, chosen because lipid tails are chemically equivalent to alkanes. This force field reproduces the experimental density (0.728 g/cm^3) and liquid–vapor surface tension (23 mN/m) of decane at 300 K with essentially quantitative agreement (simulated values 0.727 g/cm^3 and 23 mN/m) [45]. The lipid components (i.e., the monolayer and bilayer) were generated and equilibrated with the CHARMM-GUI Membrane Builder [51]. Simulations of bilayers were conducted in a box of size 7 nm × 7 nm × 10 nm (containing 150 lipids and ≈11,000 water molecules).

To model the solid surface, we adopted the setup from our previous works [17,45]. The surface consisted of two self-assembled monolayers (SAMs) with lateral dimensions of 10.4 nm × 10.3 nm, with their hydrophobic sides joined together. Each SAM was composed of 504 hydroxyl-terminated (-OH) alkyl chains (i.e., *n*-decanols) modeled with the CHARMM36 force field, arranged in a hexagonal lattice with a lattice constant of 0.497 nm, and stabilized by harmonic restraints. This structure thus represents an atomically smooth surface.

To render the surface fully hydrophobic, we set the polarity of the OH groups to zero by switching off their partial charges, achieving a contact angle of approximately 115° [17]. Although a methyl-terminated SAM would be chemically more realistic, with a slightly higher contact angle [52], we opted for the nonpolar OH-terminated variant to build on our previous studies, which systematically examined the role of surface polarity [17,45]. In fact, the precise chemical identity of terminal groups (and thus the contact angle) has only minimal influence on lipid monolayer adhesion, as lipid tails are nonpolar and thus interact with the surface almost entirely via dispersion forces [45]. Since dispersion forces scale with substrate atom density, which varies only within a narrow range for most biological and polymeric materials (≈0.7–0.9 g/cm^3), our model captures the generic behavior of lipid adhesion on smooth organic surfaces [45].

The simulation box extended around 11 nm in the z-direction and contained 1008 decanol (SAM) molecules, 332 lipids, and ≈ 20,000 water molecules. Prior to pressure-ramp simulations, the systems were equilibrated for 3 ns at 1 bar. The equilibrated configurations were then used as starting points for the pressure-ramp simulations.

2.2. Simulation details

The MD simulations were conducted using Gromacs 2022.1, with a timestep of 2 fs. Bonds involving hydrogen atoms were constrained with the LINCS algorithm, enabling stable integration. Periodic boundary conditions were applied in all three spatial directions. Both electrostatic and LJ interactions were treated with PME methods, employing a real-space cutoff of 1.4 nm [53,54]. The system temperature was maintained at 300 K using the v-rescale thermostat [55] with a time constant of 0.1 ps. Pressure was controlled with the C-rescale barostat [56] with a time constant of 1 ps and a compressibility of 4.5×10^{-5} bar^{-1}. As shown previously [22], the specific choice of barostat does not significantly affect the cavitation behavior. The pressure coupling was applied along the z-direction (normal to the surface or membrane) only, while the lateral box dimensions were kept fixed. Nevertheless, the water phase experiences an isotropic negative pressure, as expected for a liquid.

2.3. Pressure ramp method

Cavitation is a stochastic process that requires overcoming a free energy barrier, G^*. The rate of cavitation events is described by reaction rate theory [22,57] as

$$k = k_0 \mathrm{e}^{-\beta G^*} \tag{1}$$

where $\beta = 1/(k_\mathrm{B}T)$, k_B is the Boltzmann constant, and T is the absolute temperature. The kinetic prefactor k_0 represents the attempt frequency for nucleation, while the exponential factor reflects the probability of overcoming the free energy barrier at a given pressure.

Directly measuring the cavitation rate k from simulations at constant negative pressure is generally impractical due to the long waiting times involved. To circumvent this challenge, we employed a pressure-ramp protocol, as introduced in our earlier works [14,17,22].

In this method, the pressure is decreased linearly in time as $p(t) = \dot{p}t$, where $\dot{p} < 0$ denotes the pressure ramp rate. As the pressure drops, the free energy barrier $G^*(t)$ gradually decreases, eventually reaching a point where cavitation is likely to occur within the accessible simulation time. The corresponding pressure p^*_cav, denoted with an asterisk, is referred to as the *dynamic cavitation pressure*. Note that the latter should not be confused with the cavitation pressure, p_cav, which represents the cavitation limit under constant-pressure conditions and is ultimately estimated using CNT.

The pressure ramp, $p(t)$, renders the cavitation rate $k(t)$ in Eq. (1) time-dependent. Solving the time-dependent rate equations [22] yields an expression for the dynamic cavitation pressure, p^*_cav:

$$p^*_\mathrm{cav} = \dot{p} \int_0^\infty \mathrm{e}^{-k_0 I(t)}\,\mathrm{d}t \tag{2}$$

where

$$I(t) = \int_0^t \mathrm{e}^{-\beta G^*(t')}\,\mathrm{d}t' \tag{3}$$

and $G^*(t)$ is the barrier height at time-dependent pressure $p(t)$. The kinetic theory (Eq. (2)) predicts the mean pressure, p^*_cav, at which cavitation occurs during a pressure ramp, and captures its dependence on the ramp rate.

Since GROMACS does not directly support time-dependent pressure control, we approximated the ramp by running a sequence of short simulations at fixed pressures that decrease incrementally. A cavitation event was identified by a sudden jump in system volume, as shown in the example in Fig. S1 in the Supplementary Material.

All input files required to reproduce the simulations are openly available in the data repository (see Data Availability).

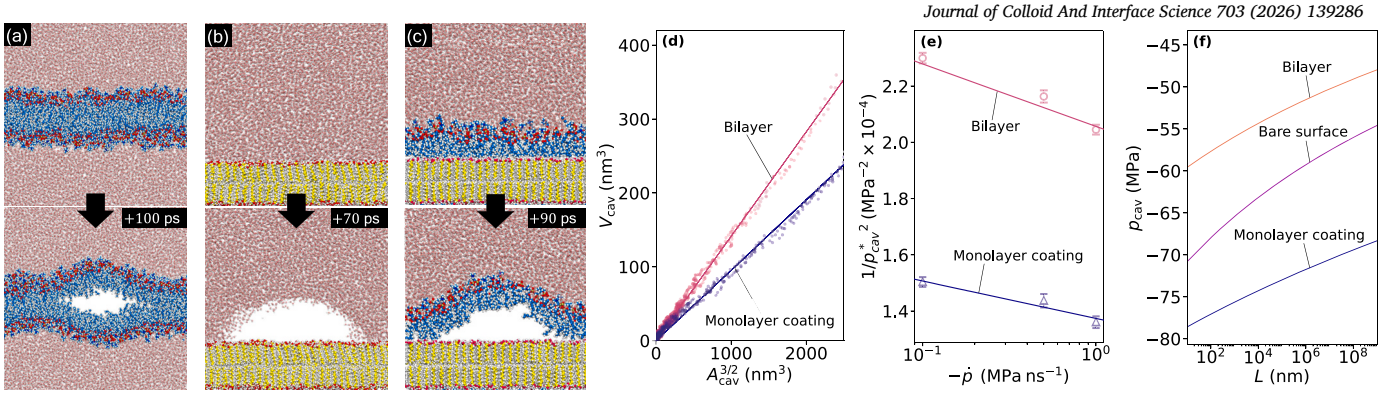

Fig. 2. Snapshots from pressure-ramp simulations showing cavitation in (a) a lipid bilayer (at $p^*_{cav} = -68$ MPa), (b) a bare planar hydrophobic surface (at $p^*_{cav} = -88$ MPa), and (c) a lipid-coated hydrophobic surface (at $p^*_{cav} = -84$ MPa). The top panels show the systems immediately before cavitation, and the bottom panels show the subsequent bubble growth. Each snapshot represents a vertical cross-section through the cavity center. (d) Correlation between the cavity volume (V_{cav}) and the cross-sectional area of the cavity ($A_{cav}^{3/2}$) obtained from 5 independent simulations of a lipid bilayer and a lipid-coated surface. Lines represent linear fits to the data with α_{ll} and α_{ls} as fitting parameters. (e) Mean dynamic cavitation pressures from pressure-ramp simulations of a lipid bilayer and of a lipid-coated surface, plotted against the pressure rate (symbols). Each data point is averaged over 10 independent simulations. Solid lines represent fits based on the kinetic theory (Eq. (2)), with k_0 as the fitting parameter, providing κ_{ll} and κ_{ls}. (f) Cavitation pressures computed using CNT parameterized with simulation data for the three systems: a lipid bilayer in water (Eq. (8)), a bare atomically smooth hydrophobic surface in contact with water (computed in Ref. [17]), and a lipid-coated hydrophobic surface in contact with water (Eq. (10)). Results are shown as a function of the lateral dimension L for a square system ($L \times L$) and a fixed observation time of $\tau = 1$ s.

3. Results and discussion

3.1. Cavitation of a lipid bilayer

We begin by examining cavitation in a lipid bilayer in water under negative pressure (Fig. 1d). This system was previously investigated in our earlier work [22]. Here, we revisit the underlying free energy concepts and perform new simulations of a DLPC lipid bilayer using an improved and more reliable force field (see the Methods section) [58]. While the qualitative conclusions remain the same, our updated simulations yield significant quantitative corrections.

As the negative pressure decreases in a ramp simulation, it eventually reaches the point at which the two leaflets of the bilayer separate, forming a lens-shaped cavity (Fig. 2a). To extend these results to static conditions and larger system sizes beyond the reach of simulations, we adopt a theoretical framework inspired by CNT. While originally developed for homogeneous liquids [59], CNT can be extended to soft materials such as lipid bilayers by properly defining the interfacial work and geometry. To this end, the free energy of the cavity within the bilayer is expressed as [22]

$$G_{ll} = w_{ll} A_{cav} + p V_{cav} \tag{4}$$

The first term represents the surface free energy required to create a cavity with cross-sectional area A_{cav} (i.e., the surface of lost contacts between lipid tails of the two leaflets), where w_{ll} is the lipid–lipid (ll) adhesion tension. The second term accounts for the energy gained during cavity expansion of volume V_{cav} under negative pressure p.

The cavity volume and cross-sectional area are evaluated from our simulations; see Section S2 of the Supplementary Material for methodological details. The results, shown in Fig. 2d as V_{cav} versus $A_{cav}^{3/2}$, indicate an empirical relationship of the form $V_{cav} = \alpha_{ll} A_{cav}^{3/2}$, where α_{ll} is a dimensionless geometric factor characterizing the cavity shape. A linear fit to the data yields $\alpha_{ll} = 0.14$—slightly larger than the value $\alpha_{ll} = 0.11$ reported in our previous work [22].

The free energy barrier for cavitation (corresponding to the maximum of G_{ll} in Eq. (4)) is given by [22]

$$G^*_{ll} = \frac{4}{27} \frac{w_{ll}^3}{\alpha_{ll}^2 p^2} \tag{5}$$

and the critical cavity lateral area at this barrier is

$$A^*_{cav} = \left(\frac{2 w_{ll}}{3 \alpha_{ll} p} \right)^2 \tag{6}$$

According to the reaction rate theory (Eq. (1)), the rate of cavitation events within a bilayer of dimensions $L \times L$ is expressed as

$$k_{ll} = \kappa_{ll} L^2 e^{-\beta G^*_{ll}} \tag{7}$$

The prefactor represents the frequency of cavitation "attempts" in the bilayer, with κ_{ll} being the areal density of this attempt frequency (i.e., average number of attempts per area and time), which will be determined by our simulations.

Although cavitation could, in principle, also occur in the surrounding water via homogeneous nucleation at a rate k_w, this process requires much lower pressures and is therefore negligible compared to cavitation within the bilayer ($k_w \ll k_{ll}$). The mean time it takes for the first cavitation event to occur is given by $\tau = k_{ll}^{-1}$ [57].

We define the *cavitation pressure* as the pressure at which cavitation occurs within an observation time τ. The corresponding expression is obtained from Eqs. (5) and (7) as [22]

$$p_{cav} = -\sqrt{\frac{4 w_{ll}^3}{27 k_B T \alpha_{ll}^2 \ln(\kappa_{ll} L^2 \tau)}} \tag{8}$$

As seen, the adhesion tension w_{ll} and geometric factor α_{ll} are the key parameters governing the cavitation pressure. The former is obtained from simulations by gradually separating two lipid leaflets and integrating the resulting interleaflet force (see Section S3 of the Supplementary Material). At ambient pressure ($p \approx 0$), we obtain $w_{ll} \approx 50$ mN/m, about twice the value of the surface tension of alkanes (23–28 mN/m) [60]. This is expected since lipid tails behave similarly to liquid alkanes, which validates the value of w_{ll} obtained with the current force field. Under negative pressure, the adhesion decreases slightly to $w_{ll} \approx 47$ mN/m at -50 MPa because the applied tension slightly separates the two leaflets (see Fig. S3b for the full $w_{ll}(p)$ dependence). Accounting for this weak pressure dependence is essential for accurate evaluation, which renders Eq. (8) implicit in p_{cav}.

Finally, to compute p_{cav} from Eq. (8), we have to determine the attempt frequency density, κ_{ll}, from pressure-ramp simulations. These yield the mean dynamic cavitation pressures, p^*_{cav}, as a function of pressure rate, shown as symbols in Fig. 2e. The data are fitted with the kinetic theory (Eq. (2)), using $k_0 = \kappa_{ll} A_{xy}$ as the fitting parameter, where A_{xy} is the lateral simulation box area. The resulting fit, shown as a solid line, gives $\kappa_{ll} = 2.62 \times 10^{14}$ s^{-1} nm^{-2}. Although the cavitation rate in the

Table 1
Simulation-derived parameters used in CNT calculations.

System	Parameter values
Lipid bilayer	$w_{ll} = 44$–47 mN/m[†]
	$\kappa_{ll} = 2.62 \times 10^{14}$ s^{-1} nm^{-2}
	$\alpha_{ll} = 0.141$
Lipid–surface (no pits)	$w_{ls} = 41$–46 mN/m[‡]
	$\kappa_{ls} = 1.76 \times 10^{15}$ s^{-1} nm^{-2}
	$\alpha_{ls} = 0.097$
Lipid–surface (with pits)	$\kappa_{pit}(1\text{ nm}) = 5.1 \times 10^{20}$ s^{-1}
	$\alpha_{pit}(1\text{ nm}) = 0.093$
	$\kappa_{pit}(2\text{ nm}) = 1.2 \times 10^{23}$ s^{-1}
	$\alpha_{pit}(2\text{ nm}) = 0.096$

[†] For $p \approx -60$ to -50 MPa; full $w_{ll}(p)$ curve in Fig. S3b.
[‡] For $p \approx -80$ to -70 MPa; full $w_{ls}(p)$ curve in Fig. S3b.

simulations scales linearly with the interfacial area, A_{xy}, the extracted intensive parameter κ_{ll} is independent of the system size, as explicitly demonstrated elsewhere [22]. In all simulations, the lateral box dimensions were chosen large enough to accommodate the critical cavity.

With all the necessary parameters at hand (Table 1), Eq. (8) allows us to compute the cavitation pressure of a lipid bilayer of various areas L^2 for a waiting time of $\tau = 1$ s. The results, shown in Fig. 2f, indicate that across bilayer sizes from $L = 10$ nm to 1 m, the cavitation pressure remains within a narrow range of -60 to -50 MPa. A similar weak dependence holds for the waiting time, as both L and τ appear within a logarithm in Eq. (8). This weak dependence on size and time is a general characteristic of cavitation, allowing the cavitation pressure to be approximately treated as a length- and time-scale independent intensive material property, akin to tensile strength.

The uncertainty in CNT-based cavitation pressures is governed by w_{ll} and α_{ll}. While the statistical errors of these simulation-derived parameters are only a few percent, we do not propagate them into formal error bars of p_{cav}, as the total uncertainty is dominated by systematic factors (e.g., multiscale CNT approximations, force-field accuracy). Nevertheless, these systematic effects do not alter the relative trends, which remain robust across all systems examined.

The cavitation pressures for lipid bilayers obtained in the present work are approximately seven times higher in magnitude than those reported in our earlier study [22]. This discrepancy originates from the Berger lipid force field used in the previous work, which underestimated lipid–lipid cohesion between alkyl tails. In contrast, the CHARMM36 force field employed here quantitatively reproduces alkane surface tensions and thus provides a reliable description of lipid–lipid adhesion tension, w_{ll}. Despite this quantitative difference, our earlier qualitative conclusion remains valid: lipid bilayers are significantly less stable than pure water against cavitation, but they are still strong enough not to trigger cavitation at the pressures typically found in plants (several MPa) [1,8].

3.2. Cavitation at smooth lipid-free and lipid-coated surfaces

Building on the insights from cavitation in lipid bilayers, we now turn to cavitation at smooth hydrophobic surfaces, modeled as atomistically smooth SAMs; see the Methods section. Before we discuss the influence of the lipid coating, we first recapitulate heterogeneous cavitation at a bare SAM in water, which has been analyzed in our previous work [17]. A representative snapshot of a cavitation event is shown in Fig. 2b, where a vapor bubble in the shape of a spherical cap nucleates at the surface. The cavitation pressures, computed via CNT (for details see our previous work [17]), are plotted in Fig. 2f. These results indicate that cavitation at the bare hydrophobic surface occurs at slightly lower pressures than in lipid bilayers of equal area. This similarity in cavitation pressures arises because the lipid–lipid adhesion tension, w_{ll}, is comparable to the work required to remove a water layer from the solid surface. The latter is given by the Young–Dupré equation as $\gamma_w(1 + \cos\theta) \approx 42$ mN/m, assuming a surface tension of $\gamma_w = 68$ mN/m for TIP4P/2005 water and a contact angle of $\theta = 115°$.

In the next step, we use the same SAM, place a lipid monolayer on top, and equilibrate the system at atmospheric pressure to allow the monolayer to adsorb to the SAM. We assume the same area per lipid as in the bilayer, noting that small variations have a negligible impact on adhesion because of the liquid-like nature of the lipid tails [45]. During the subsequent pressure ramp simulations, the lipid monolayer first remains adsorbed to the surface, as shown in Fig. 2c (upper panel). Density profiles of water and lipids (see Section S4 in the Supplementary Material) decrease only slightly—by a few percent—as expected from the low compressibility of these phases, with no indication of significant structural changes near the interface. This indicates that cavitation onset is not preceded by interfacial reorganization or drying, but occurs via a sudden nucleation event, whose likelihood increases steeply as the pressure approaches the critical value p^*_{cav}. At this point, the monolayer locally detaches from the surface, forming a half-lens-shaped cavity, as shown in Fig. 2c (bottom panel). This detachment closely resembles the cavitation observed in bilayers (Fig. 2a), albeit only in one half-space.

Because of this similarity, we can reuse the theoretical framework developed for bilayers (Eqs. (4)–(8)) by substituting the relevant quantities from the lipid–lipid (ll) to the lipid–surface (ls) case: $w_{ll} \to w_{ls}$, $\alpha_{ll} \to \alpha_{ls}$, and $\kappa_{ll} \to \kappa_{ls}$. The key geometric difference—where the cavity forms a half-lens rather than a full lens—is fully captured by the parameter α_{ls}, which accounts for the altered surface-to-volume ratio of the cavity.

In analogy to Eqs. (7) and (8), the cavitation rate and pressure for a monolayer adsorbed to a smooth surface follow as

$$k_{ls} = \kappa_{ls} L^2 e^{-\beta G^*_{ls}} \tag{9}$$

and

$$p_{cav} = -\sqrt{\frac{4 w_{ls}^3}{27 k_B T \alpha_{ls}^2 \ln(\kappa_{ls} L^2 \tau)}} \tag{10}$$

The lipid–surface adhesion tension, w_{ls}, for this system was evaluated in our previous work [45] and reanalyzed here (Section S3 in the Supplementary Material). We found that w_{ls} slightly depends on the applied pressure, and that $w_{ls} \approx w_{ll}$, which aligns with expectations since adhesion between the substrate and lipid tails is primarily governed by dispersion interactions, just as in the adhesion between two lipid leaflets.

In Fig. 2d, we plot the relationship between cavity volume and area during monolayer cavitation. A fit to the data gives a geometric factor $\alpha_{ls} = 0.097$. As expected, this value is smaller than α_{ll} for bilayers, since the cavity beneath a monolayer film can only expand upward, unlike in a bilayer, where the cavity expands in both directions.

Finally, the attempt frequency density is obtained by fitting the pressure-ramp data in Fig. 2e (with $k_0 = \kappa_{ls} A_{xy}$ as the fitting parameter) yielding $\kappa_{ls} = 1.76 \times 10^{15}$ s^{-1} nm^{-2}. Using this value in Eq. (10), we compute the cavitation pressures for a lipid monolayer adsorbed on a solid surface; shown in Fig. 2f. The pressures span a range from -80 and -70 MPa across a wide range of monolayer areas.

Interestingly, these pressures are lower (i.e., more negative) than those for bilayers and those for bare hydrophobic surfaces. This slightly larger stability compared to bilayers is expected, primarily because the monolayer forms a smaller cavity volume during cavitation for a given areal detachment ($\alpha_{ls} < \alpha_{ll}$), making it more resistant against cavitation.

In our previous work [45], it was established that in aqueous systems, lipids adsorb onto smooth surfaces with contact angles above approximately $\theta_{adh} \approx 65°$, while excess lipids self-assemble into bilayers in the bulk. Building on this, the results in Fig. 2f show that under such conditions, the bilayers—not the coated surfaces—become the weakest structural component, exhibiting slightly lower resistance to cavitation than bare atomically smooth hydrophobic surfaces.

In other words, for defect-free containers with hydrophobic walls, adding lipids (or other amphiphiles) to the aqueous medium does not

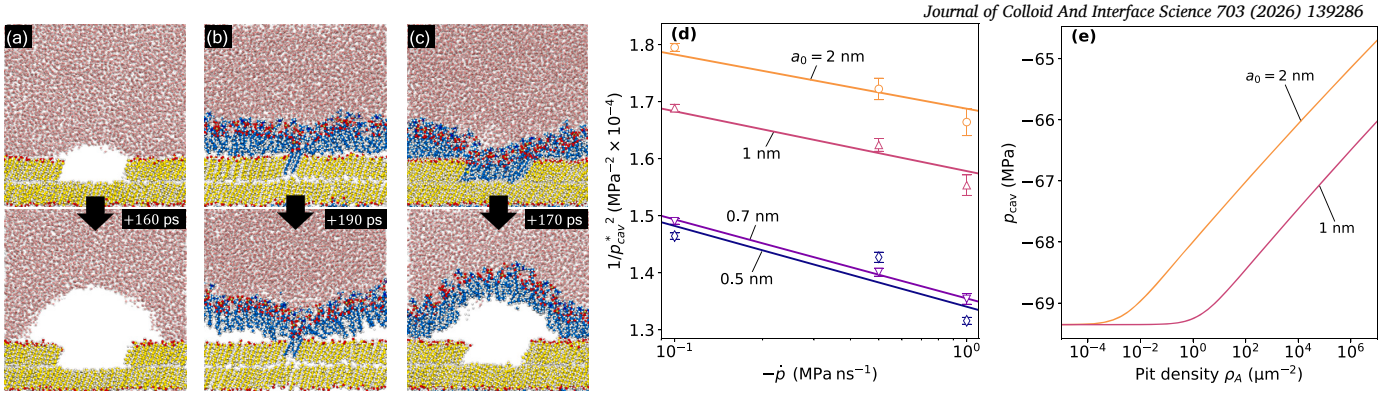

Fig. 3. (a) Metastable vapor nanobubble spontaneously formed inside a hydrophobic nanopit of radius 2 nm. As the ramping pressure reaches $p^*_{cav} = -45$ MPa (top panel), the bubble abruptly spreads over the surface, triggering cavitation (bottom panel). Adapted from Ref. [17]. (b) Lipid monolayer adsorbed on a surface with a nanopit of radius $a_0 = 0.5$ nm (top snapshot). During pressure-ramp simulations (at $p^*_{cav} = -84$ MPa), cavitation consistently initiates on the smooth surface region rather than at the nanopit (bottom snapshot). (c) Same system with a larger nanopit ($a_0 = 2$ nm). Here, cavitation nucleates at the nanopit during the pressure ramp (at $p^*_{cav} = -77$ MPa). (d) Mean dynamic cavitation pressures from pressure-ramp simulations of lipid-coated surfaces with nanopits of different radii (indicated by labels), plotted against the pressure ramp rate (symbols). Each data point is averaged over 10 independent simulations. Solid lines represent fits based on the kinetic theory (Eq. (2)), with $k = \kappa_{pit} A_{xy}$ as the fitting parameter, yielding κ_{pit}. (e) Cavitation pressure of a lipid-coated hydrophobic surface of lateral size $L = 1$ m as a function of pit density ρ_A, shown for pit radii of 1 and 2 nm (as indicated); computed using Eq. (13).

enhance cavitation resistance but does not significantly compromise it either.

3.3. Lipid-coated surfaces with nanopits

Up to this point, our analysis has focused on idealized, atomically smooth hydrophobic surfaces. In reality, however, surfaces are rarely defect-free; they often feature cracks, crevices, and other topographic irregularities. It is important to distinguish between gently undulating topographies—smooth at the molecular scale—and sharp nanoscale defects. While the former are unlikely to interfere with lipid monolayer adsorption, the latter could disrupt its continuity, especially where the monolayer must bend sharply to conform to the underlying surface.

To probe the impact of such nanoscale roughness, we introduce cylindrical nanometer-sized pits—referred to as *nanopits*—into our SAM model. The pits are created by removing decanol molecules from one of the SAMs within a specified radius ($a_0 = 0.5$, 0.7, 1, and 2 nm) [17].

The cavitation behavior of such nanopits without lipids was investigated in our previous work [17]. As shown in the equilibrated snapshot in Fig. 3a, water does not enter the nanopit because its hydrophobic interior undergoes spontaneous dewetting [61]. A simple free-energy estimate (see Section S5 in the Supplementary Material) supports the expectation that hydrophobic cylindrical pits of the studied dimensions indeed remain dry at ambient, or at least mildly negative, pressures. The resulting vapor pocket is thermodynamically stable at ambient conditions but becomes metastable under tension, acting as a weak spot that readily triggers cavitation once the pressure drops below a critical threshold.

As a next step, we place a lipid monolayer onto the surface. After equilibration at atmospheric pressure, the simulation snapshots in Fig. 3b and c (top) show that the monolayer tightly conforms to the nanopits: the lipids fill the cavity and eliminate any voids. This is a crucial observation, as it suggests that lipid monolayer films can effectively seal nanoscale topographical defects, thereby preventing the formation of trapped gas or vapor pockets that would otherwise act as cavitation nuclei.

The ability of the lipid monolayer to conform to and fill the nanopit arises from a balance between two competing factors: adhesion, which favors coverage of exposed surfaces, and monolayer deformation energy, which resists it. For wider pits, deformation is primarily due to bending (Fig. 3c); for narrower pits, protrusion becomes the dominant mode (Fig. 3b). In our case, adhesion always appears to prevail.

We can estimate the relevant energetic contributions. Prior to monolayer deformation, the nanopit beneath resembles a cylindrical cavity, consisting of exposed alkyl tails of SAM decanols and lipid tails at the top. Its surface area is given by $A = 2\pi a_0(a_0 + h)$, where h is the cavity height. When the monolayer fills the nanopit, the exposed hydrophobic surfaces are eliminated, resulting in an adhesion energy gain of $W_{adh} = \gamma_{hc} A$, where $\gamma_{hc} \approx 25$ mN/m is the surface tension of hydrocarbons. For a representative nanopit with $a_0 \approx h \approx 1$ nm, this gives $W_{adh} \approx 80\, k_B T$. The cost of bending the monolayer to conform to the pit can be approximated by modeling the pit as a hemispherical cavity. The associated bending energy is $W_b = 4\pi\kappa_b$, where κ_b is the bending rigidity of the monolayer [62]. Requiring that the gain in adhesion energy outweigh the cost of bending, $W_b < W_{adh}$, leads to the condition $\kappa_b \lesssim 6\, k_B T$, which falls within a realistic range for lipid monolayers.

We next investigate the stability of lipid-covered nanopits against cavitation using pressure-ramp simulations. For the smaller nanopits ($a_0 \lesssim 0.7$ nm), the monolayer film is pinned to the pit and detaches from the smooth regions of the surface, as shown in Fig. 3b (bottom). Consequently, the dynamic cavitation pressures (p^*_{cav}) are indistinguishable from those of a lipid-coated defect-free surface (Fig. 3d). This means that lipid-coated sub-nanometer defects have a negligible impact on cavitation resistance—at least at low defect densities. In contrast, for the larger nanopits ($a_0 \gtrsim 1$ nm), cavitation occurs at the nanopit (Fig. 3c). These nanopits thus act as weak spots where cavitation is more likely to occur. As a result, p^*_{cav} is slightly higher than for surfaces with smaller nanopits or no nanopits at all (Fig. 3d).

To quantify the cavitation rate at a lipid-covered nanopit, we express the free energy barrier for cavitation as $G^*_{pit}(p) = G^*_{ls}(p) + \Delta G_{pit}$, where G^*_{ls} represents the free energy barrier of a smooth lipid-covered surface, and ΔG_{pit} is a free energy correction due to the nanopit. We assume that ΔG_{pit} is independent of pressure, allowing us to absorb this term into the kinetic prefactor, $\kappa_{pit}(a_0)$, which simplifies the cavitation rate expression to

$$k_{pit} = \kappa_{pit}(a_0) e^{-\beta G^*_{ls}} \tag{11}$$

In other words, cavitation at the lipid-covered nanopit follows the same fundamental behavior as on a smooth surface but with a modified prefactor that accounts for the nanopit. This approach is expected to work only when the nanopit size is smaller than the critical cavity size of the smooth lipid-coated surface, A^*_{cav}. From Eq. (6) (with ll → ls) we find $A^*_{cav} \approx 15$ nm^2, corresponding to a critical cavity radius of about 2.2 nm.

The simulations indicate that the proportionality constant α_{pit}, which relates the cavitation cross-sectional area to the cavity volume, is essentially the same as for the defect-free surface, $\alpha_{\mathrm{pit}} \approx \alpha_{\mathrm{ls}}$ (see Table 1 and Fig. S2c in the Supplementary Material). We therefore assume $\alpha_{\mathrm{pit}} = \alpha_{\mathrm{ls}}$ in the following analysis.

The kinetic prefactor κ_{pit} is determined from pressure-ramp simulations by fitting the kinetic theory (Eq. (2)) to the cavitation pressures for each nanopit size separately, as shown in Fig. 3d. The resulting values are summarized in Table 1. Notably, the pressure-ramp simulations already reveal that a lipid-coated nanopit is significantly more resistant to cavitation than an uncoated one—a difference we will analyze more quantitatively in the following section.

To do so, we first extend the model to describe cavitation on a surface containing N identical nanopits. In this case, cavitation can occur through one of two possible pathways: it can initiate either at one of the nanopits or on the surrounding smooth regions of the surface. The total cavitation rate is therefore the sum of all the contributions

$$k = k_{\mathrm{ls}} + N k_{\mathrm{pit}} \tag{12}$$

where k_{ls} is the cavitation rate for the smooth surface (Eq. (9)) and k_{pit} accounts for cavitation at an individual nanopit (Eq. (11)). We assume that the total area covered by the nanopits is much smaller than the smooth portion of the surface ($N\pi a_0^2 \ll L^2$), ensuring that the surface cavitation rate on the defect-free surface, k_{ls}, remains virtually unchanged.

It is convenient to introduce the nanopit density, $\rho_A = N/L^2$ (the number of nanopits per unit area). Using this, the cavitation pressure for a system with nanopits follows from Eq. (12) as

$$p_{\mathrm{cav}} = -\sqrt{\frac{4\omega_{\mathrm{ls}}^3}{27 k_{\mathrm{B}} T \alpha_{\mathrm{ls}}^2 \ln\left[(\kappa_{\mathrm{ls}} + \kappa_{\mathrm{pit}}\rho_A) L^2 \tau\right]}} \tag{13}$$

In the limiting case of $\rho_A = 0$ (i.e., no nanopits), the equation reduces to Eq. (10), recovering the cavitation pressure for a smooth lipid-coated surface.

The resulting cavitation pressures as a function of nanopit density, for radii $a_0 = 1$ nm and $a_0 = 2$ nm on a hydrophobic surface with linear dimension $L = 1$ m, are shown in Fig. 3e. The pressure behavior exhibits a clear crossover: at low nanopit densities, cavitation occurs mainly on the smooth regions of the surface, and the nanopits have little to no impact. As the nanopit density increases, the nanopits become cavitation nuclei, crossing over to a nanopit-dominated regime. However, even when the nanopit density is high ($\rho_A \approx 10^6$ μm^{-2}), the increase in cavitation pressure remains modest—only a few MPa, corresponding to a relative change of just a few percent.

These results demonstrate that lipid monolayers effectively stabilize liquids against cavitation under negative pressure, even in the presence of densely distributed nanoscale defects. The observed cavitation pressures ($p_{\mathrm{cav}} \approx -65$ MPa) are comparable to those for uncoated, defect-free surfaces ($p_{\mathrm{cav}} \approx -55$ MPa; Fig. 2f), and significantly more negative than those for uncoated surfaces with defects, as discussed next.

3.4. Cavitation in the presence of mesoscale pits

We now turn to surface defects with larger radii—ranging from tens of nanometers to microns—which are expected to greatly reduce the cavitation resistance. According to classical crevice models, larger pits trap larger bubbles, making them more effective cavitation nuclei.

Although atomistic simulations cannot directly access such mesoscale geometries, they still offer valuable insights. Lipid adsorption is governed by local surface structure rather than the absolute size of the pit. Importantly, since larger pits locally resemble flat surfaces, it is reasonable to extrapolate our nanoscale findings and argue that lipids will also coat and passivate larger pits.

To illustrate this concept, consider a cubic water-filled container of size L with smooth walls and rounded edges and corners; the latter is to exclude additional effects from sharp corners. One of the walls contains a single hydrophobic pit of radius a_0, which hosts a vapor bubble, as illustrated in Fig. 4a. We only consider a single pit, as our prior work showed that cavitation is governed by the largest pit rather than by their number [17]. Thus, the pit in this model serves as a representative of the largest bubble-hosting feature in the system.

The behavior of this system is described by the total cavitation rate, which includes contributions from bulk water, flat surfaces, and pit-trapped bubbles, $k = k_{\mathrm{w}} + k_{\mathrm{s}} + k_{\mathrm{pit}}$ (details are provided in Ref. [17]).

Fig. 4c shows the cavitation pressure as a function of pit radius for smooth hydrophilic ($\theta = 0°$) and hydrophobic ($\theta = 115°$) walls without lipids. For sub-nanometer pits, cavitation occurs either in the bulk (for hydrophilic walls) or on flat hydrophobic surfaces. However, once $a_0 \gtrsim 1$ nm, the bubble in the pit becomes the dominant nucleation site and dramatically elevates the cavitation pressure.

For larger pits (above several nanometers), the cavitation pressure asymptotically approaches the simple mechanical stability criterion [17],

$$p_{\mathrm{cav}} \approx p_{\mathrm{vap}} - \frac{2\gamma_{\mathrm{w}}}{a_0} \tag{14}$$

on hydrophilic walls ($\theta < 90°$) and

$$p_{\mathrm{cav}} \approx p_{\mathrm{vap}} - \frac{2\gamma_{\mathrm{w}}}{a_0}\sin\theta \tag{15}$$

on hydrophobic walls ($\theta > 90°$). Here, p_{vap} stands for the saturated vapor pressure (~ 2–3 kPa at ambient temperatures) and γ_{w} is again the water surface tension. These expressions highlight the drastic reduction in tensile strength caused by larger surface crevices. While sub-10-nanometer pits can withstand negative pressures of several tens of MPa, cavitation sets in at just a few MPa beyond ~10 nm, and rises above −1 MPa for pits larger than ~100 nm.

Although our study focuses on vapor cavities, gas-filled bubbles (e.g., air bubbles) exhibit similar expansion dynamics, with corrections arising from gas pressure in Eqs. (14) and (15). For more details, we refer the interested reader to Refs. [21,24,63].

Lipid adsorption dramatically changes the situation. When present in sufficient quantities, lipids coat hydrophobic surfaces, including rough or concave nanoscale features, rendering them effectively hydrophilic, which is critical because hydrophilic pits cannot host nanobubbles. This sealing mechanism removes Harvey-type nuclei (see Fig. 4b for an illustration). Once surface defects are passivated, the cavitation threshold is no longer determined by bubble expansion but by the stability of the remaining lipid structures—typically the bilayers in the bulk, which are formed by the excess of lipids. These bilayers can resist negative pressures down to around −60 to −50 MPa, depending on their area (plotted as a shaded band in Fig. 4c). For comparison, the darker shaded band in Fig. 4c represents the cavitation pressure of lipid-coated surfaces, with the width reflecting the variation due to nanoscale corrugation (based on our nanopit analysis in Fig. 3e). These values are significantly more negative than the cavitation pressure induced by uncoated mesoscale surface defects, highlighting the effectiveness of lipid coatings.

These findings have important implications for understanding water transport in vascular plants. According to Eq. (14), a single uncoated hydrophobic crevice with a radius of 50 nm can trigger cavitation at a pressure of −3 MPa—a pressure commonly encountered in plant xylem [1,8]. Notably, xylem walls often contain structural irregularities such as helical thickenings, warts, pits, and vestures, many of which extend up to several micrometers [31,32,64,65]. Yet, plants routinely sustain such negative pressures without frequent failure. Our results offer a possible explanation: lipids naturally present in xylem sap may adsorb to hydrophobic patches in vessel walls and seal off potential nucleation sites. By doing so, lipids shift the limiting factor from bubble-hosting defects to more robust structures like bilayers or other lipid aggregates. This mechanism provides a plausible and physically grounded explanation for how plants can suppress cavitation and maintain long-distance water transport under negative pressure.

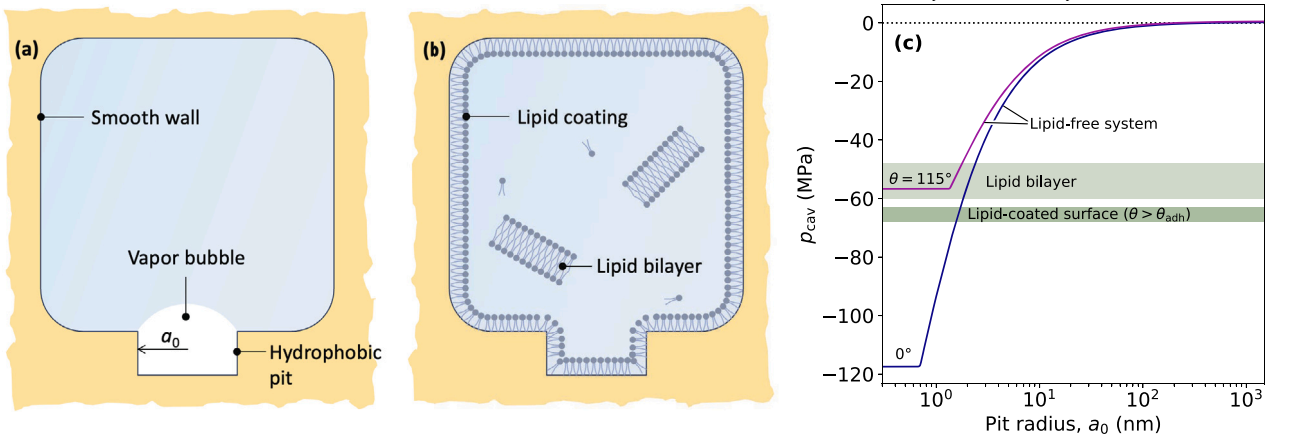

Fig. 4. Cavitation suppression by lipid coatings. (a) Schematic of a cubic container with smooth hydrophobic walls (yellow) filled with water (blue), featuring rounded edges and a single hydrophobic surface pit of radius a_0. In the absence of lipids, the pit hosts a vapor bubble (white), which acts as a Harvey-type cavitation nucleus. (b) The same system, now with excess lipids that form bilayers in the bulk and adsorb onto the walls and the pit, rendering the walls effectively hydrophilic and eliminating the trapped vapor bubble. (c) Cavitation pressure as a function of pit radius for a container of size $L = 1$ m. Solid lines show the cavitation threshold for lipid-free systems (panel a) with hydrophilic ($\theta = 0°$) and hydrophobic ($\theta = 115°$) walls, based on kinetic theory with a 1 s observation time, as computed in Ref. [17]. Shaded green bands represent the cavitation pressure range for systems with lipids (panel b): the lighter band corresponds to bilayer cavitation (excess lipids, spanning areas from 100 nm^2 to 1 m^2) and the darker band to lipid-coated walls (with contact angles above the adhesion threshold $\theta_{adh} \approx 65°$ [45,46]). In lipid-rich systems, cavitation is no longer dominated by pit-hosted bubbles (solid lines) but by bilayer stability (shaded bands). (For interpretation of the colors in the figure(s), the reader is referred to the web version of this article.)

4. Conclusions

This study reveals a new mechanism by which amphiphilic molecules stabilize liquids under negative pressure: lipid adsorption onto hydrophobic surface defects passivates nanobubble-hosting cavities, thereby eliminating the dominant cavitation nuclei. Using a multiscale approach, linking molecular dynamics simulations with classical nucleation theory, we show that once such sites are sealed, cavitation resistance shifts to the weakest remaining component—lipid bilayers or aggregates, which withstand substantially higher tensions than trapped nanobubbles.

The reality of biological and soft-matter interfaces—such as chemical heterogeneity, lipid mixtures, and dynamic adsorption—undoubtedly adds further layers of complexity. Nonetheless, our idealized framework provides a molecular-level explanation for long-standing experimental observations that trace amounts of surfactants or polymers can suppress cavitation in aqueous systems [33–36]. This protective mechanism, however, is remarkably vulnerable: surface coverage must be nearly perfect. If even a single hydrophobic crevice remains uncoated and traps a bubble, it can serve as a nucleation site, making the passivation of all other sites irrelevant. This all-or-nothing nature is intrinsic to cavitation and helps explain why lipid protection is difficult to demonstrate experimentally, given the slow dynamics and incomplete adsorption of lipids.

Such a protective mechanism may operate in plant xylem, where lipids coat vessel walls and passivate crevices to prevent cavitation and embolism formation [1,8,32]. A recent study suggested that freezing in xylem sap may originate from nanoscale crevices that dewet under tension [66]. Our findings imply that lipid coatings could likewise help prevent sap freezing by stabilizing these crevices against dewetting. Over time, lipid depletion and redistribution could expose defects, helping explain conduit aging and hydraulic vulnerability [67–69].

Beyond plants, this work establishes a general principle of interfacial stabilization: amphiphile coatings can deactivate cavitation nuclei and extend liquid metastability. This insight suggests practical strategies for suppressing cavitation in microfluidics, biomedical devices, and soft materials, where cavitation limits performance or causes erosion [38].

Future work should aim at experimental validation. In plant xylem, controlled depletion or modification of amphiphile layers could directly test the link between lipid coatings and cavitation resistance. More generally, lipid adsorption could be examined on model surfaces (e.g., by AFM, cryo-EM), and cavitation thresholds could be measured in microfluidic systems with well-defined amphiphile coverage.

CRediT authorship contribution statement

Marin Šako: Writing – original draft, Visualization, Investigation, Formal analysis. **Steven Jansen:** Writing – review & editing, Conceptualization. **H. Jochen Schenk:** Writing – review & editing, Conceptualization. **Roland R. Netz:** Writing – review & editing, Methodology, Conceptualization. **Emanuel Schneck:** Writing – review & editing, Conceptualization. **Matej Kanduč:** Writing – review & editing, Writing – original draft, Supervision, Project administration, Investigation, Funding acquisition, Conceptualization.

Declaration of competing interest

The authors declare that they have no known competing financial interests or personal relationships that could have appeared to influence the work reported in this paper.

Acknowledgements

M.Š. and M.K. acknowledge financial support from the Slovenian Research and Innovation Agency (ARIS) (contracts P1-0055 and J1-4382).

Appendix A. Supplementary material

Supplementary material related to this article can be found online at https://doi.org/10.1016/j.jcis.2025.139286.

Data availability

Simulation files are available at https://doi.org/10.5281/zenodo.15529899. Python scripts for setting up and analyzing pressure ramp simulations are available at https://doi.org/10.5281/zenodo.14678800.

References

[1] A.D. Stroock, V.V. Pagay, M.A. Zwieniecki, N. Michele Holbrook, The physicochemical hydrodynamics of vascular plants, Annu. Rev. Fluid Mech. 46 (2014) 615–642.

[2] X. Noblin, N. Rojas, J. Westbrook, C. Llorens, M. Argentina, J. Dumais, The fern sporangium: a unique catapult, Science 335 (2012) 1322.
[3] V.E. Vinogradov, P.A. Pavlov, The boundary of limiting superheats of n-heptane, ethanol, benzene, and toluene in the region of negative pressures, High Temp. 38 (2000) 379–383.
[4] T.D. Wheeler, A.D. Stroock, The transpiration of water at negative pressures in a synthetic tree, Nature 455 (2008) 208–212.
[5] O. Vincent, D.A. Sessoms, E.J. Huber, J. Guioth, A.D. Stroock, Drying by cavitation and poroelastic relaxations in porous media with macroscopic pores connected by nanoscale throats, Phys. Rev. Lett. 113 (2014) 134501.
[6] I.-T. Chen, D.A. Sessoms, Z. Sherman, E. Choi, O. Vincent, A.D. Stroock, Stability limit of water by metastable vapor–liquid equilibrium with nanoporous silicon membranes, J. Phys. Chem. B 120 (2016) 5209–5222.
[7] S. Datta, R. Pillai, M.K. Borg, K. Sefiane, Acoustothermal nucleation of surface nanobubbles, Nano Lett. 21 (2021) 1267–1273.
[8] B. Choat, et al., Global convergence in the vulnerability of forests to drought, Nature 491 (2012) 752–755.
[9] F. Caupin, E. Herbert, Cavitation in water: a review, C. R. Phys. 7 (2006) 1000–1017.
[10] E. Herbert, S. Balibar, F. Caupin, Cavitation pressure in water, Phys. Rev. E 74 (2006) 041603.
[11] F. Caupin, A.D. Stroock, The stability limit and other open questions on water at negative pressure, Liq. Polymorph. 152 (2013) 51–80.
[12] M.E.M. Azouzi, C. Ramboz, J.-F. Lenain, F. Caupin, A coherent picture of water at extreme negative pressure, Nat. Phys. 9 (2013) 38–41.
[13] G. Menzl, M.A. Gonzalez, P. Geiger, F. Caupin, J.L. Abascal, C. Valeriani, C. Dellago, Molecular mechanism for cavitation in water under tension, Proc. Natl. Acad. Sci. USA 113 (2016) 13582–13587.
[14] M. Šako, R.R. Netz, M. Kanduč, Impact of nanoscopic impurity aggregates on cavitation in water, Surf. Interf. 62 (2025) 106243.
[15] Q. Zheng, D. Durben, G. Wolf, C. Angell, Liquids at large negative pressures: water at the homogeneous nucleation limit, Science 254 (1991) 829–832.
[16] P. Loche, M. Kanduč, E. Schneck, R.R. Netz, Water cavitation results from the kinetic competition of bulk, surface, and surface-defect nucleation events, Phys. Fluids 37 (2025).
[17] M. Šako, F. Staniscia, R.R. Netz, E. Schneck, M. Kanduč, Nanoscale defects and heterogeneous cavitation in water, J. Mol. Liq. 431 (2025) 127797.
[18] J.C. Fisher, The fracture of liquids, J. Appl. Phys. 19 (1948) 1062–1067.
[19] F. Caupin, Liquid-vapor interface, cavitation, and the phase diagram of water, Phys. Rev. E 71 (2005) 051605.
[20] E.N. Harvey, D. Barnes, W.D. McElroy, A.H. Whiteley, D. Pease, K. Cooper, Bubble formation in animals. I. Physical factors, J. Cell. Physiol. 24 (1944) 1–22.
[21] B.M. Borkent, S. Gekle, A. Prosperetti, D. Lohse, Nucleation threshold and deactivation mechanisms of nanoscopic cavitation nuclei, Phys. Fluids 21 (2009).
[22] M. Kanduč, E. Schneck, P. Loche, S. Jansen, H.J. Schenk, R.R. Netz, Cavitation in lipid bilayers poses strict negative pressure stability limit in biological liquids, Proc. Natl. Acad. Sci. USA 117 (2020) 10733–10739.
[23] R.T. Knapp, Cavitation and nuclei, J. Basic Eng. 80 (1958) 1315–1324.
[24] A.A. Atchley, A. Prosperetti, The crevice model of bubble nucleation, J. Acoust. Soc. Am. 86 (1989) 1065–1084.
[25] D. Lohse, A. Prosperetti, Homogeneous nucleation: patching the way from the macroscopic to the nanoscopic description, Proc. Natl. Acad. Sci. USA 113 (2016) 13549–13550.
[26] S. Jones, G. Evans, K. Galvin, Bubble nucleation from gas cavities—a review, Adv. Colloid Interface Sci. 80 (1999) 27–50.
[27] F. Caupin, Escaping the no man's land: recent experiments on metastable liquid water, J. Non-Cryst. Solids 407 (2015) 441–448.
[28] W. Lauterborn, R. Mettin, in: J.A. Gallego-Juárez, K.F. Graff, M. Lucas (Eds.), Power Ultrasonics, second edition, in: Woodhead Publishing Series in Electronic and Optical Materials, Woodhead Publishing, 2023, pp. 23–52.
[29] J. Kehr, A. Buhtz, P. Giavalisco, Analysis of xylem sap proteins from Brassica napus, BMC Plant Biol. 5 (2005) 1–13.
[30] H.J. Schenk, S. Espino, D.M. Romo, N. Nima, A.Y. Do, J.M. Michaud, B. Papahadjopoulos-Sternberg, J. Yang, Y.Y. Zuo, K. Steppe, et al., Xylem surfactants introduce a new element to the cohesion-tension theory, Plant Physiol. 173 (2017) 1177–1196.
[31] M. McCully, M. Canny, A. Baker, C. Miller, Some properties of the walls of metaxylem vessels of maize roots, including tests of the wettability of their lumenal wall surfaces, Ann. Bot. 113 (2014) 977–989.
[32] H.J. Schenk, S. Espino, S.M. Rich-Cavazos, S. Jansen, From the sap's perspective: the nature of vessel surfaces in angiosperm xylem, Am. J. Bot. 105 (2018) 172–185.
[33] J. Creech, V. Divino, W. Patterson, P.J. Zalesky, C.E. Brennen, A remarkable example of bubble nucleation suppression, in: Proceedings of the JSME Mechanical Engineering Congress, Tokyo, Japan, 2002, 28–24 September, 2002, pp. 24–28.
[34] L. Crum, J. Gallemore, D. Nordling, Effect of surface tension on the cavitation threshold of water, J. Acoust. Soc. Am. 52 (1972) 151–152.
[35] L.A. Crum, Nucleation and stabilization of microbubbles in liquids, Appl. Sci. Res. 38 (1982) 101–115.
[36] L.A. Crum, J.E. Brosey, Effect of dilute polymer additives on the acoustic cavitation threshold of water, J. Fluids Eng. 106 (1984) 99–104.
[37] S. Bhandari, P. Kang, J. Jeong, J. Cao, K. Ehmann, Cavitation bubble removal by surfactants in laser-induced plasma micromachining, Manuf. Lett. 32 (2022) 96–99.
[38] M. Abedini, S. Hanke, On the reasons for reduced cavitation erosion of alloys in water containing SDS and NaCl, Wear (2025) 205792.
[39] F. Vera, R. Rivera, D. Romero-Maltrana, J. Villanueva, Negative pressures and the first water siphon taller than 10.33 meters, PLoS ONE 11 (2016) e0153055.
[40] F.M. Scott, V. Sjaholm, E. Bowler, Light and electron microscope studies of the primary xylem of Ricinus communis, Am. J. Bot. 47 (1960) 162–173.
[41] K. Esau, V. Cheadle, R. Gill, Cytology of differentiating tracheary elements II. Structures associated with cell surfaces, Am. J. Bot. 53 (1966) 765–771.
[42] J. Lahiri, S.J. Jonas, A.G. Frutos, P. Kalal, Y. Fang, Lipid microarrays, Biomed. Microdevices 3 (2001) 157–164.
[43] P. Lenz, C.M. Ajo-Franklin, S.G. Boxer, Patterned supported lipid bilayers and monolayers on poly (dimethylsiloxane), Langmuir 20 (2004) 11092–11099.
[44] C.B. Babayco, S. Turgut, A.M. Smith, B. Sanii, D. Land, A.N. Parikh, A comparison of lateral diffusion in supported lipid monolayers and bilayers, Soft Matter 6 (2010) 5877–5881.
[45] M. Šako, F. Staniscia, E. Schneck, R.R. Netz, M. Kanduč, Conditions for the stable adsorption of lipid monolayers to solid surfaces, PNAS Nexus 2 (2023) pgad190.
[46] M. Kanduč, E. Schneck, R.R. Netz, Understanding the "Berg limit": the 65° contact angle as the universal adhesion threshold of biomatter, Phys. Chem. Chem. Phys. 26 (2024) 713–723.
[47] J.L.F. Abascal, C. Vega, A general purpose model for the condensed phases of water: TIP4P/2005, J. Chem. Phys. 123 (2005) 234505.
[48] W. Wagner, A. Pruß, The IAPWS formulation 1995 for the thermodynamic properties of ordinary water substance for general and scientific use, J. Phys. Chem. Ref. Data 31 (2002) 387–535.
[49] K. Vanommeslaeghe, E. Hatcher, C. Acharya, S. Kundu, S. Zhong, J. Shim, E. Darian, O. Guvench, P. Lopes, I. Vorobyov, et al., CHARMM general force field: a force field for drug-like molecules compatible with the CHARMM all-atom additive biological force fields, J. Comput. Chem. 31 (2010) 671–690.
[50] A. Botan, et al., Toward atomistic resolution structure of phosphatidylcholine headgroup and glycerol backbone at different ambient conditions, J. Phys. Chem. B 119 (2015) 15075–15088.
[51] S. Jo, T. Kim, V.G. Iyer, W. Im, CHARMM-GUI: a web-based graphical user interface for CHARMM, J. Comput. Chem. 29 (2008) 1859–1865.
[52] S.R. Carlson, R.R. Netz, Subnanometer interfacial hydrodynamics: spatially resolved viscosity and surface friction, Nano Lett. (2025), https://doi.org/10.1021/acs.nanolett.5c03950.
[53] U. Essmann, L. Perera, M.L. Berkowitz, T. Darden, H. Lee, L.G. Pedersen, A smooth particle mesh Ewald method, J. Chem. Phys. 103 (1995) 8577–8593.
[54] C.L. Wennberg, T. Murtola, S. Páll, M.J. Abraham, B. Hess, E. Lindahl, Direct-space corrections enable fast and accurate Lorentz–Berthelot combination rule Lennard-Jones lattice summation, J. Chem. Theory Comput. 11 (2015) 5737–5746.
[55] G. Bussi, D. Donadio, M. Parrinello, Canonical sampling through velocity rescaling, J. Chem. Phys. 126 (2007) 014101.
[56] M. Bernetti, G. Bussi, Pressure control using stochastic cell rescaling, J. Chem. Phys. 153 (2020) 114107.
[57] P. Hänggi, P. Talkner, M. Borkovec, Reaction-rate theory: fifty years after Kramers, Rev. Mod. Phys. 62 (1990) 251.
[58] Y. Yu, A. Kramer, R.M. Venable, B.R. Brooks, J.B. Klauda, R.W. Pastor, CHARMM36 lipid force field with explicit treatment of long-range dispersion: parametrization and validation for phosphatidylethanolamine, phosphatidylglycerol, and ether lipids, J. Chem. Theory Comput. 17 (2021) 1581–1595.
[59] P.G. Debenedetti, Metastable Liquids: Concepts and Principles, 1996.
[60] J.J. Jasper, E.V. Kring, The isobaric surface tensions and thermodynamic properties of the surfaces of a series of n-alkanes, C5 to C18, 1-alkenes, C6 to C16, and of n-decylcyclopentane, n-decylcyclohexane and n-decylbenzene, J. Phys. Chem. 59 (1955) 1019–1021.
[61] K. Lum, D. Chandler, J.D. Weeks, Hydrophobicity at small and large length scales, J. Phys. Chem. B 103 (1999) 4570–4577.
[62] U. Seifert, Configurations of fluid membranes and vesicles, Adv. Phys. 46 (1997) 13–137.
[63] M.A. Chappell, S.J. Payne, The effect of cavity geometry on the nucleation of bubbles from cavities, J. Acoust. Soc. Am. 121 (2007) 853–862.
[64] S. Jansen, P. Baas, P. Gasson, E. Smets, Vestured pits: do they promote safer water transport?, Int. J. Plant Sci. 164 (2003) 405–413.
[65] A. Costa, A.C. Wiedenhoeft, On the possible functions of helical thickenings in conductive cells in wood, IAWA J. 44 (2023) 381–398.
[66] S. Ingram, A. Zanetti, L. Mustonen, A.A. Piedehierro, A. Laaksonen, A. Lintunen, Toward understanding apoplastic freezing under negative pressure, New Phytol. (2025).
[67] K. Fukuda, D. Kawaguchi, T. Aihara, M.Y. Ogasa, N.H. Miki, T. Haishi, T. Umebayashi, Vulnerability to cavitation differs between current-year and older xylem: non-destructive observation with a compact magnetic resonance imaging system of two deciduous diffuse-porous species, Plant Cell Environ. 38 (2015) 2508–2518.
[68] C.R. Brodersen, A.B. Roddy, J.W. Wason, A.J. McElrone, Functional status of xylem through time, Annu. Rev. Plant Biol. 70 (2019) 407–433.
[69] J.C. Fickle, W.R. Anderegg, et al., Ring-specific vulnerability to embolism reveals accumulation of damage in the xylem, New Phytol. 246 (2025) 2046.